IEEE Access
Multidisciplinary | Rapid Review | Open Access Journal

Received May 22, 2021, accepted June 6, 2021, date of publication June 14, 2021, date of current version June 24, 2021.

Digital Object Identifier 10.1109/ACCESS.2021.3089197

Improved Damping Control Method for Grid-Forming Converters Using LQR and Optimally Weighted Feedback Control Loops

MOHAMED AHMED[1], FAHAD ALSOKHIRY[2], (Member, IEEE), AYMAN S. ABDEL-KHALIK[3,4], (Senior Member, IEEE), KHALED H. AHMED[4], (Senior Member, IEEE), AND YUSUF AL-TURKI[2]

[1]Department of Engineering Mathematics and Physics, Alexandria University, Alexandria 21544, Egypt
[2]Department of Electrical and Computer Engineering, Faculty of Engineering, King Abdulaziz University, Jeddah 21589, Saudi Arabia
[3]Department of Electrical Engineering, Alexandria University, Alexandria 21544, Egypt
[4]Department of Electronic and Electrical Engineering, University of Strathclyde, Glasgow G1 1XQ, U.K.

Corresponding author: Mohamed Ahmed (mohamed.abuyehia@alexu.edu.eg)

This work w as supported by the Deputyship for Research and Innovation, the Ministry of Education in Saudi Arabia, under Project 1071.

ABSTRACT Power grid pattern is expected to evolve from generator-based power systems towards converter-based systems in the forthcoming decades. Therefore, grid-forming converters will be pertinent to interconnected power grids in pursuance of enhancement their resilience against disturbances. This paper introduces a new efficient damping control method for grid-forming converters that provides a smooth power modulation and an efficient damping response against frequency and voltage deviations. First, an averaged state-space representation for a grid forming application in dq synchronization frame is derived. Based on this model, a new hybrid damping controller, including the concept of state feedback control and PI control, is proposed to address the main issues in existing controllers. The state feedback controller is optimally designed using a linear-quadratic regulator (LQR) approach to optimize the system performance. Moreover, the PI controller is optimally designed using the pattern search algorithm. The proposed damping control method integrates optimally between the control loops through a mapping matrix to rapidly synchronize with the grid and efficiently damp the oscillations. Simulations are carried out to prove the proposed method robustness. Finally, a comparative study using controller hardware-in-the-loop (CHiL) is employed against conventional system to validate the proposed damping method.

INDEX TERMS Grid-forming converters, inverter dominated grid, weak grid, virtual inertia, damping emulation, distributed generation, LQR design, pattern search.

I. INTRODUCTION

Synchronous machine (SM) is one of the most prominent equipment in the conventional power grid, due to its significant contributions for preserving the grid stability against load disturbances [1]. Moreover, it provides valuable characteristics, which can be summed up as follows [2]: (i) The synchronizing torque, which is produced when the rotor speed deviates from the synchronous speed in an endeavor to bring it back to the synchronization. It is provided by the excitation system, rotating mass inertia and/or other internal control loops. (ii) The damping torque, which is provided by the damper windings and plays an important role during disturbances. Insufficient both synchronizing and damping torques will lead to non-oscillatory and oscillatory instabilities, respectively.

The tendency to transmute from generator-based power systems towards power electronics converter-based systems (due to large renewable energy integration) has substantial consequences on power system stability due to the shortcomings of the total system inertia and damping energy [1]–[3]. Therefore, recent research activities have attempted to control the grid-tied converters in a manner that emulates the behavior of SMs by adapting them to serve as grid-forming converters (GFC) instead of grid-following converters. To this end, different promising techniques have been proposed, such

The associate editor coordinating the review of this manuscript and approving it for publication was Zhilei Yao.

as droop-based grid-forming control methods [4], [5], virtual synchronous machine (VSM) [6]–[8], synchronverter [9], virtual oscillator control [10], voltage-controlled inverter [11], matching control [12]–[15], power synchronization control [16], and direct power control [17].

The inner control structure for the GFCs is usually implemented using conventional PI controllers thanks to their simplicity. However, there are many other control structures that have been alternatively proposed for grid-connected converters, for instance, fuzzy logic control [18], Sliding-Mode and Mixed H2/H∞ Control [19], and neural network-based control [20]. These control techniques aim to design a robust controller to achieve a better performance in terms of settling time. However, these techniques are complex and require very high computations [21].

Damping effect can be inherently included in the control of grid-forming converters via various forms. In early stages of GFC [22], damping effect has been addressed by employing a seventh order SM model. However, this strategy is very complex and provides inadequate damping responses under certain disturbances. Then, it has been investigated widely two main approaches, namely: VSM based damping methods and matching control based damping method. For VSM based damping methods, the GFC can operate as a controlled voltage source through two main loops (P-f control loop) and (Q-V control loop), where the damping effect can be included into any of such loops. Therefore, the first category of damping methods, which is more dominant, utilizes the damping into (P-f loop) with numerous ways. For instance, the method given in [11] has applied the difference between the virtual speed (frequency) and the nominal speed. However, this method influences the steady state performance including inertia response and governor functions. Another method has been introduced in [23], which depends on the difference between the virtual speed and the measured one from the phase lock loop (PLL). This method does not influence the inertia response, nevertheless, PLL cannot properly operate in weak grids, which might cause instability problems. Another method presented in [24], [25] has applied the virtual speed derivative or the active power with suitable filters for damping purposes. However, this method needs a tricky filter design to achieve strong damping without affecting the inertia response and steady state operating conditions. The method given in [26], has employed the concept of a forward power (or angle feedforward). This method promotes self-synchronization; however, it provides inadequate damping response under some operational cases. Finally, the method introduced in [27] has achieved the required damping through a high pass filter; however, the filter design is complex and based on a compromise between the damping response and system stability phase margin. For the second category of damping methods, Q-V control loop has been used to include the damping effect. The idea was inspired by the power system stabilizer. The power system stabilizer uses an additional control signal to the excitation system control loop to address the negative impact of decreasing the damping torque in SM while improving the synchronizing torque. For instance, the method in [28] has used a damping correction loop in synchronverter control to adjust its dynamic response, however, it includes a complex seventh order SM model. The method presented in [29] has applied the filtered virtual speed to the Q-V control loop, however, a second-order filter must be finely designed.

In some application where the real power loop is not fully accessible by the controller. Therefore, the inertia and damping are provided based on the dynamics of the DC-link and the P-f control loop is replaced by a DC-link voltage control loop. These controllers are widely known as matching control in literature. For instance, the method in [14], which has utilized the damping into the DC-link voltage control loop, however it includes a PLL which provides an improper damping action during the weak grid conditions.

From the discussion above, it is a quite clear from literature that the two main shortcomings in previous damping control methods are no damping technique has been designed specifically for weak grid conditions and no universal damping control method could include all advantages from previous methods simultaneously without compromising on level of control complexity, inertia response, and implementation simplicity.

This paper proposes a simple GFC controller that optimally combine three damping concepts, namely, the damping through Q-V control loop as in power system stabilizer (PSS) and power oscillation damping (POD) in Static Synchronous Series Compensator (SSSC), the damping through P-f control loop as in certain types of VSMs, and the damping through the DC-link dynamics as illustrated in the matching control method. Therefore, it significantly improves the transient responses through a sufficient damping against a wide range of disturbances without deteriorating the inertia as well as the steady state response. Moreover, the proposed GFC model deals efficiently with the weak grid conditions, as it does not rely on the PLL. In addition, it considers the interference between P-f and Q-V loops, which depends on the R/X ratio.

The key contributions are summarized as follows:

- Proposing a new hybrid damping controller, including three damping concepts to address the main limitations in existing controllers.
- Designing an optimal state-feedback controller using a linear quadratic regulator (LQR) approach to compromise between the control efforts and the speed of system responses for GFC applications.
- Developing a new mapping matrix using pattern search optimization algorithm, which provides the optimum cross coupling between the control loops.

This paper is organized as follows. In Section II, the previous damping strategies, which related to the proposed damping technique, are reviewed. The state-space model is derived in Section III. Section IV describes the proposed control scheme. Section V covers the optimal design of control parameters using LQR and pattern search algorithm for developing the mapping matrix. The robustness analysis

of the proposed controller against uncertain parameters is discussed. The results are presented in Section VI using the Control Hardware in the Loop via the OPAL-RT real time simulator.

II. CONVENTIONAL DAMPING METHODS

This section reviews the prevailing damping techniques, which are related strongly to the proposed control scheme. As previously discussed, the damping strategy can be integrated within any of the two control loops (P-f and Q-V), as VSM-based method, or through controlling the DC-link dynamics as in matching control-based method. These two approaches are briefly reviewed since they provide the basic principle of the proposed control.

A. VSM BASED DAMPING APPROACH

The recent control strategy for VSM [8], which depends on the modified version of the swing equation (1), can integrate the damping through three different methods, as shown in Fig. 1.

$$J\frac{d\omega_m}{dt} + \frac{1}{\omega_n}P_{damp} = \frac{1}{\omega_n}\left(P_{ref} - P_o\right) \tag{1}$$

where, J is the inertia constant, ω_m is the estimated speed, ω_n is the nominal speed, ω_g is the grid speed, P_{damp}, P_{ref}, P_o are the damping power, reference power, and converter output power, respectively. D represents the damping coefficient.

The damper can be represented as an active power component (P_{damp}), which is proportional to the difference between the ω_m and ω_n, or between the ω_m and ω_g, or the derivative of ω_m, as shown in Fig. 1(a). These techniques generally deteriorate the inertia response. Furthermore, employing PLL as a frequency measurement unit causes instability problems in case of weak grids. Therefore, the common tendency to mitigate this problem is to add a damping speed term (ω_{damp}), as in Fig. 1(b). However, it is not effective in VSMs, where the inertia is emulated by the DC-link capacitor [8]. Moreover, it is more effective to use the voltage magnitude v_{damp} to provide damping as in power system stabilizer. However, the main challenge will be the adjustment of the transfer function($G_{damp(S)}$) to achieve the required damping, as in Fig. 1(c).

B. MATCHING CONTROL BASED DAMPING APPROACH

The fundamental concept behind the matching control is the duality between the DC-link voltage and angular velocity dynamics [30], as shown in Fig. 2, and described by (2).

$$i_{dc} - i_{inv} = C_{dc}\frac{dv^{cap}}{dt} \tag{2}$$

Equation (2) can be further written as (3) by multiplying with $\mathbf{v^{cap}}$.

$$p_{dc} - p_{inv} = \frac{C_{dc}}{2}\frac{d\,(v^{cap})^2}{dt} \tag{3}$$

where, i_{dc}, p_{dc} are the input DC-link current and DC power, respectively, i_{inv}, p_{inv} are the input inverter current and power, respectively.

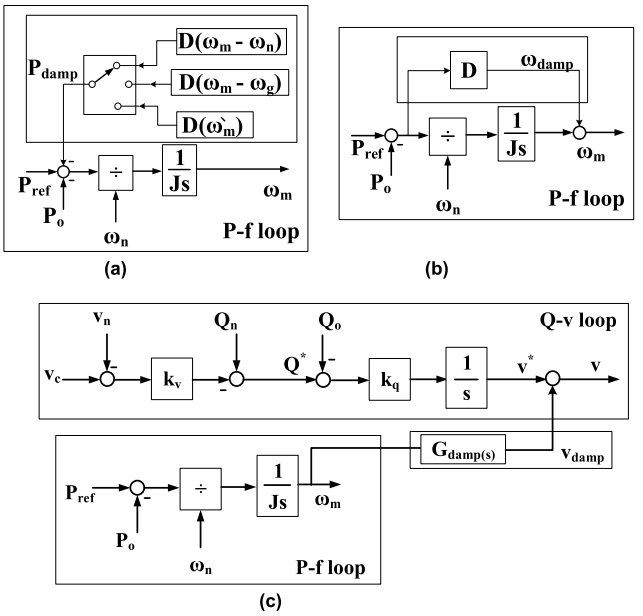

FIGURE 1. Damping schemes for VSM: (a) Active power damping, (b) Angular speed damping, and (c) Voltage damping.

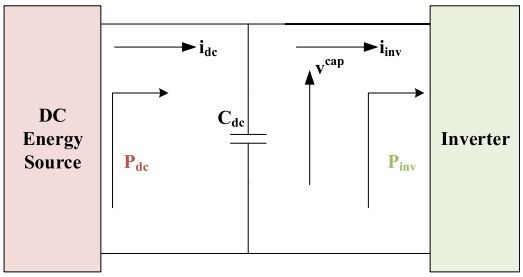

FIGURE 2. Inertia emulation by matching control.

Moreover, the DC-link voltage controller can be used to control the dc-link voltage in order to track a specific reference and also works as a grid synchronization unit as discussed in [14] and described by (4).

$$\omega^* = \omega_g + \frac{s + K_t}{K_j s + K_d}\left[\left(v^{cap}\right)^2 - v_{ref}^2\right] \tag{4}$$

where, K_d, K_j and K_t are the damping coefficient, inertia emulation coefficient, and voltage tracking coefficient, respectively.

Equation (3) can be reformulated as (5) by substituting in (4), which indicates that the inertia and damping emulation can be achieved by tracking the voltage over the DC-capacitor.

$$\underbrace{-\left(p_{dc} - p_{inv}\right) + \underbrace{\frac{K_d C_{dc}}{2}\left(\omega_m - \omega_g\right)}_{damping\ term} + \frac{K_j C_{dc}}{2}s\omega_m}_{Grid\ synchronization\ component} = \underbrace{\frac{K_t C_{dc}}{2}\left[v_{ref}^2 - \left(v^{cap}\right)^2\right]}_{DC-voltage\ tracking\ component} \tag{5}$$

General control block diagram for the conventional GFC is shown in Fig. 3, which summarizes the major control loops for the two previous control approaches. It can be seen clearly that the damping can be included in any of the three loops P-f control, Q-V control, and DC-link control. The majority of the grid-forming converter controllers in literature depends only on one of such loops to generate the damping effect. Therefore, the proposed control method introduces the damping effect and the emulated inertia based on an information from the three predefined control loops, besides, it uses the DC-link voltage loop to regulate the DC-link voltage.

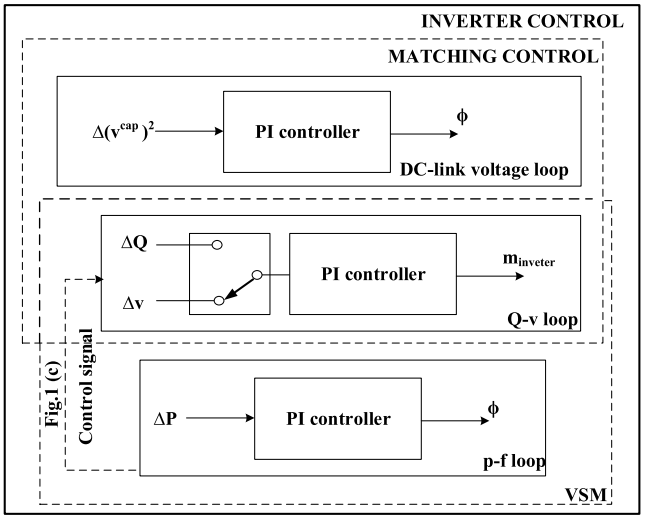

FIGURE 3. Conventional control loop schemes.

III. STATE-SPACE MODELLING OF GRID-TIED CONVERTERS

This section discusses the proposed system structure and derives the state-space averaged model employed in this study.

A. SYSTEM STRUCTURE

The overall system structure for a two-stage grid-connected converter is shown in Fig. 4. It comprises a DC-DC converter, which regulates the DC-link voltage, followed by a grid connected inverter operating as a grid-forming converter with an LCL output filter interfacing. The converter is modulated by a space vector pulse width modulation (SVPWM). In the grid-following mode, the DC-DC converter extracts the maximum power from the renewable source. The inverter just tracks the grid voltage, while operating as a current source to inject the extracted power into the grid. In contrast, the roles are swapped with the grid in grid-forming mode, where the inverter operates as a variable voltage source with internally generated reference frequency (not measured). Under this latter mode, the inverter adjusts its power output automatically based on grid conditions, then the DC-DC converter tracks this required power to regulate the DC-link voltage.

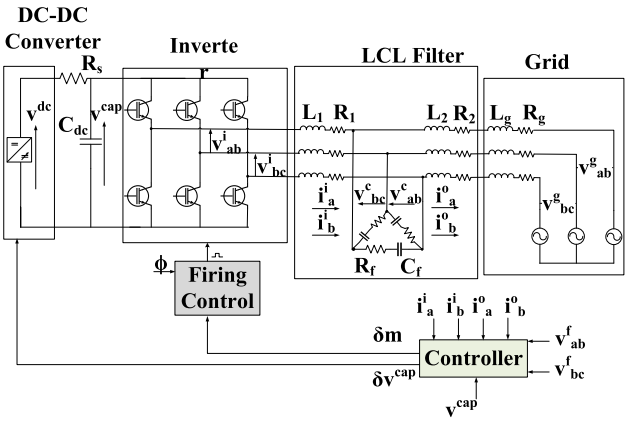

FIGURE 4. The overall system structure for the two-stage grid-connected system.

B. STATE-SPACE MODELLING

The state-space averaged model of the grid-connected converter is obtained through three steps. First, the SVPWM converter has six sectors with six active switching states and two zero states. Each switching state corresponds to a certain linear circuit and has its own state-space matrix (A), which ends up to 8 state-space matrices ($A_0 - A_7$) corresponding to all possible circuits with different switching states, as shown in Fig. 5. Consequently, the averaged state-space matrices ($\bar{A}_I - \bar{A}_{VI}$) can be obtained by averaging the corresponded three state-space matrices over one switching cycle, T_s.

For instance, the average state-space matrix in sector one ($\bar{A}_I$) over T_s can be expressed as in (6).

$$\bar{A_I} = d_0A_0 + d_1A_1 + d_2A_2 \tag{6}$$

where, d_0, d_1, and d_2 are given by (7) and represent the duty cycles of the three state-space matrices A_0, A_1 and A_2, respectively, given in the appendix, m is the modulation index for SVPWM, and θ is the angle of the voltage for the LCL capacitor.

$$\begin{aligned} d_1 &= msin(\pi/3 - \theta) \\ d_2 &= msin(\theta) \\ d_0 + d_1 + d_2 &= 1 \end{aligned} \tag{7}$$

The averaged state-space representation in the rotating abc frame for sector 1 can be described in (8), as shown at the bottom of the next page, where v^{cap} is the DC-link voltage, i_a and i_b are the input phase currents of the LCL filter, v^c_{ab} and v^c_{bc} are the line voltage across the capacitor of the LCL filter, i^o_a and i^o_b are the output phase current from the LCL filter, v^{dc} is the DC-DC converter output voltage and v^g_{ab}, v^g_{bc} are the line voltages for the grid. Moreover, the state space parameters are defined in TABLE 1.

The averaged state space representation of any sector in the dq frame can describe the operation of the GFC.

Therefore, studying the first sector in the dq frame is sufficient for describing the operation of the GFC in all other sectors. The state space representation in the dq frame is

$$\begin{bmatrix} v^{cap} \\ i_a \\ i_b \\ v^c_{ab} \\ v^c_{bc} \\ i^o_a \\ i^o_b \end{bmatrix}' = \overbrace{\begin{bmatrix} \frac{-1}{C_{dc}R_s} & \frac{-(d_1+d_2)}{C_{dc}} & \frac{-d_2}{C_{dc}} & 0 & 0 & 0 & 0 \\ \frac{2d_1+d_2}{3L_1} & \frac{-(3R_1+R_f)}{3L_1} & 0 & \frac{-2}{3L_1} & \frac{-1}{3L_1} & \frac{R_f}{3L_1} & 0 \\ \frac{-d_1+d_2}{3L_1} & 0 & \frac{-(3R_1+R_f)}{3L_1} & \frac{1}{3L_1} & \frac{-1}{3L_1} & 0 & \frac{R_f}{3L_1} \\ 0 & \frac{1}{3C_f} & \frac{-1}{3C_f} & 0 & 0 & \frac{-1}{3C_f} & \frac{1}{3C_f} \\ 0 & \frac{1}{3C_f} & \frac{2}{3C_f} & 0 & 0 & \frac{-1}{3C_f} & \frac{-2}{3C_f} \\ 0 & \frac{R_f}{3(L_2+L_g)} & 0 & \frac{2}{3(L_2+L_g)} & \frac{1}{3(L_2+L_g)} & \frac{-(3(R_{2+}R_g)+R_f)}{3(L_2+L_g)} & 0 \\ 0 & 0 & \frac{R_f}{3(L_2+L_g)} & \frac{-1}{3(L_2+L_g)} & \frac{1}{3(L_2+L_g)} & 0 & \frac{-(3(R_{2+}R_g)+R_f)}{3(L_2+L_g)} \end{bmatrix}}^{\overline{A_I}} \begin{bmatrix} v^{cap} \\ i_a \\ i_b \\ v^c_{ab} \\ v^c_{bc} \\ i^o_a \\ i^o_b \end{bmatrix}$$
$$+ \underbrace{\begin{bmatrix} \frac{1}{C_{dc}R_s} & 0 & 0 \\ 0 & 0 & 0 \\ 0 & 0 & 0 \\ 0 & \frac{-1}{2(L_2+L_g)} & \frac{\sqrt{3}}{6(L_2+L_g)} \\ 0 & \frac{-\sqrt{3}}{6(L_2+L_g)} & \frac{-1}{2(L_2+L_g)} \end{bmatrix}}_{B} \begin{bmatrix} v_{dc} \\ v^g_{ab} \\ v^g_{bc} \end{bmatrix} \tag{8}$$

$$\begin{bmatrix} v^{cap} \\ i^i_q \\ i^i_d \\ v^c_q \\ v^c_d \\ i^o_q \\ \underbrace{i^o_d}_{\bar{x}'} \end{bmatrix}' = \overbrace{\begin{bmatrix} \frac{-1}{C_{dc}R_s} & \frac{-\sqrt{3}Mcos(\Phi)}{2C_{dc}} & \frac{-\sqrt{3}Msin(\Phi)}{2C_{dc}} & 0 & 0 & 0 & 0 \\ \frac{\sqrt{3}Mcos(\Phi)}{3L_1} & \frac{-(3R_1+R_f)}{3L_1} & -\omega & \frac{-1}{2L_1} & \frac{\sqrt{3}}{6L_1} & \frac{R_f}{3L_1} & 0 \\ \frac{\sqrt{3}Msin(\Phi)}{3L_1} & \omega & \frac{-(3R_1+R_f)}{3L_1} & \frac{-\sqrt{3}}{6L_1} & \frac{-1}{2L_1} & 0 & \frac{R_f}{3L_1} \\ 0 & \frac{1}{2C_f} & \frac{\sqrt{3}}{6C_f} & 0 & -\omega & \frac{-1}{2C_f} & \frac{-\sqrt{3}}{6C_f} \\ 0 & \frac{-\sqrt{3}}{6C_f} & \frac{1}{2C_f} & \omega & 0 & \frac{\sqrt{3}}{6C_f} & \frac{-1}{2C_f} \\ 0 & \frac{R_f}{3(L_2+L_g)} & 0 & \frac{1}{2(L_2+L_g)} & \frac{-\sqrt{3}}{6(L_2+L_g)} & \frac{-(3(R_{2+}R_g)+R_f)}{3(L_2+L_g)} & -\omega \\ 0 & 0 & \frac{R_f}{3(L_2+L_g)} & \frac{\sqrt{3}}{6(L_2+L_g)} & \frac{1}{2(L_2+L_g)} & \omega & \frac{-(3(R_{2+}R_g)+R_f)}{3(L_2+L_g)} \end{bmatrix}}^{\overline{A_{dq}}} \begin{bmatrix} v^{cap} \\ i^i_q \\ i^i_d \\ v^c_q \\ v^c_d \\ i^o_q \\ \underbrace{i^o_d}_{\bar{x}} \end{bmatrix}$$
$$+ \underbrace{\begin{bmatrix} \frac{1}{C_{dc}R_s} & 0 & 0 \\ 0 & 0 & 0 \\ 0 & 0 & 0 \\ 0 & \frac{-1}{2(L_2+L_g)} & \frac{\sqrt{3}}{6(L_2+L_g)} \\ 0 & \frac{-\sqrt{3}}{6(L_2+L_g)} & \frac{-1}{2(L_2+L_g)} \end{bmatrix}}_{B} \begin{bmatrix} \underbrace{v_{dc}}_{u} \\ v^g_{ab} \\ v^g_{bc} \end{bmatrix} \tag{9}$$

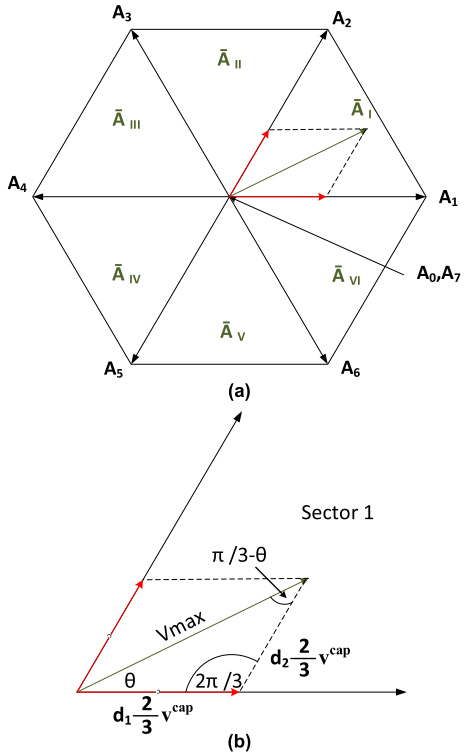

FIGURE 5. State-space representation. (a) State-space matrices for the SVPWM grid-connected converter modelling, (b) SVPWM Geometrical representation for duty cycles.

TABLE 1. System parameters.

	Grid Parameters	
ω_n	Nominal Grid Frequency	$2\pi \times 60$ rad/s
V_n	Nominal Grid Voltage	380 V
L_g	Grid Inductance	2 mH
R_g	Grid Resistance	3 Ω
	Filter and Inverter Parameters	
P	Nominal Power	65 kW
L_1, L_2	Filter Inductances	2.5 mH, 2.5 mH
C_f	Filter Capacitance	10 μF
R_1, R_2	Filter Resistances	1 mΩ, 1 mΩ,
R_f		0.7 Ω
	DC-DC Converter Parameters	
R_s	Source resistance	0.1 Ω
C_{dc}	DC-capacitance	4 mF
V_{dc}	DC-Voltage	650 V

given by (9), as shown at the bottom of the previous page, by applying the transformation in (10) and its derivative in (11).

$$\begin{bmatrix} f_a \\ f_b \end{bmatrix} = \begin{bmatrix} \cos(\theta_f) & \sin(\theta_f) \\ \cos(\theta_f - \frac{2\pi}{3}) & \sin(\theta_f - \frac{2\pi}{3}) \end{bmatrix} \begin{bmatrix} f_q \\ f_d \end{bmatrix} \tag{10}$$

$$\begin{bmatrix} f_a \\ f_b \end{bmatrix}' = \begin{bmatrix} -\theta_f' \sin(\theta_f) & \theta_f' \cos(\theta_f) \\ -\theta_f' \sin(\theta_f - \frac{2\pi}{3}) & \theta_f' \cos(\theta_f - \frac{2\pi}{3}) \end{bmatrix} \begin{bmatrix} f_q \\ f_d \end{bmatrix} + \begin{bmatrix} \cos(\theta_f) & \sin(\theta_f) \\ \cos(\theta_f - \frac{2\pi}{3}) & \sin(\theta_f - \frac{2\pi}{3}) \end{bmatrix} \begin{bmatrix} f_q \\ f_d \end{bmatrix}' \tag{11}$$

where i_q and i_d are the input dq current components of the LCL filter, v_q^c and v_d^c are the line voltage components across the capacitor of the LCL filter, i_q^o and i_d^o are the output current components from the LCL filter, θ_f is the angle between q-axis and a-axis, φ is the voltage phase difference between the grid and the GFC, which is used to control the injected active power into the grid.

Furthermore, a small perturbation (12) around the per-calculated steady-state points is introduced to generate the corresponding small-signal model and present more controllable inputs.

$$\begin{aligned} \bar{x} &= \bar{X} + \delta\bar{x} \\ \bar{u} &= \bar{U} + \delta\bar{u} \\ m &= M + \delta m \\ \varphi &= \Phi + \delta\varphi \end{aligned} \tag{12}$$

where, $\bar{x} = [v^{cap}, i_q^i, i_d^i, v_q^c, v_d^c, i_q^o, i_d^o]$ is the system state vector, $\bar{u}$ is the system input vector, and $\bar{X}, \bar{U}, M$, and Φ are the steady state operating points. The final state-space small-averaged model in the dq frame is given in (13), as shown at the bottom of the next page, where the system has 7 states and 5 inputs. The input vector (δu) includes 3 controllable inputs (δu_c) and 2 uncontrollable inputs that are considered as disturbances (δd). The controllable ones are the DC-DC converter output voltage (v^{dc}) and the power converter output voltage (v_{dq}^c). These inputs are controlled by the DC-DC converter and GFC, as shown in Fig. 6, where v^{dc} is controlled by the DC-DC converter (δv^{dc}) as shown in Fig. 5(a) and the output inverter voltage is controlled by δm and $\delta\varphi$ through SVPWM block as shown in Fig. 5(b).

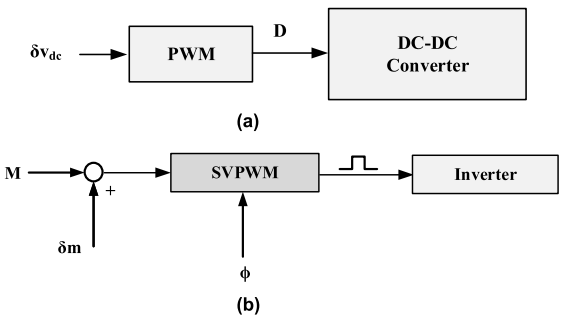

FIGURE 6. Control block diagrams for the DC-DC and grid forming converters. (a) Duty cycle calculations for DC-DC converter, (b) pulses generation for three phase GFC.

On the other hand, the uncontrollable inputs represent the dq components of the grid voltages (δv_{dq}^g).

IV. PROPOSED CONTROL METHOD

In this section, the proposed modifications to the conventional control methods are discussed. As shown in Fig. 7, the proposed control method comprises 4 PI control loops, which are:

1. DC-voltage tracking loop, which is primarily connected to δv_{dc} and regulates the voltage across the DC-link through the DC-DC converter.

2. P-f control loop, which regulates the output power and mainly connected to $\delta\varphi$ for controlling the output voltage angle and deducing the synchronization angle of Park's transformation.
3. The other two loops are the voltage control loops represented in the dq frame. Previously, the square root of these two loops is mainly used for controlling the converter modulation index, δm. However, these two signals will be used separately from each other in the proposed control method to add more resilience for the design process.

The Mapping Matrix (MM) shown in Fig. 7 consists of weighting factors, which are optimally designed along with the PI controllers' gains using a pattern search algorithm to map the PI controller outputs to generate the system input vector. The MM design will be discussed in the following section. The MM block is added to optimally attain the required coupling between the separate control loops to achieve the best system performance. For instance, in very weak grids, the frequency control is not fully handled by controlling the active power and the reactive power is not fully linked to the voltage magnitude. This cross-coupling problem between the (P-f) and (Q-V) control loops, will spontaneously be addressed by employing the proposed MM block. Moreover, it can handle the role of the power system stabilizer by providing the damping effect from the (P-f) and (Q-V) loops. As previously mentioned, the DC-link

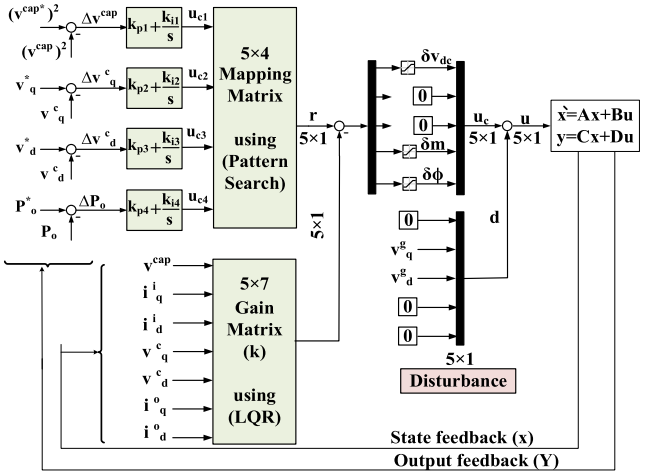

FIGURE 7. The proposed control method.

$$
\begin{bmatrix} \delta v^{cap} \\ \delta i_q^i \\ \delta i_d^i \\ \delta v_q^c \\ \delta v_d^c \\ \delta i_q^o \\ \underbrace{\delta i_d^o}_{\delta x'} \end{bmatrix}' = \overbrace{\begin{bmatrix} \frac{-1}{C_{dc}R_s} & \frac{-\sqrt{3}Mcos(\phi)}{2C_{dc}} & \frac{-\sqrt{3}Msin(\Phi)}{2C_{dc}} & 0 & 0 & 0 & 0 \\ \frac{\sqrt{3}Mcos(\Phi)}{3L_1} & \frac{-(3R_1+R_f)}{3L_1} & -\omega & \frac{-1}{2L_1} & \frac{\sqrt{3}}{6L_1} & \frac{R_f}{3L_1} & 0 \\ \frac{\sqrt{3}Msin(\Phi)}{3L_1} & \omega & \frac{-(3R_1+R_f)}{3L_1} & \frac{-\sqrt{3}}{6L_1} & \frac{-1}{2L_1} & 0 & \frac{R_f}{3L} \\ 0 & \frac{1}{2C_f} & \frac{\sqrt{3}}{6C_f} & 0 & -\omega & \frac{-1}{2C_f} & \frac{-\sqrt{3}}{6C_f} \\ 0 & \frac{-\sqrt{3}}{6C_f} & \frac{1}{2C_f} & \omega & 0 & \frac{\sqrt{3}}{6C_f} & \frac{-1}{2C_f} \\ 0 & \frac{R_f}{3(L_2+L_g)} & 0 & \frac{1}{2(L_2+L_g)} & \frac{-\sqrt{3}}{6(L_2+L_g)} & \frac{-(3(R_2+R_g)+R_f)}{3(L_2+L_g)} & -\omega \\ 0 & 0 & \frac{R_f}{3(L_2+L_g)} & \frac{\sqrt{3}}{6(L_2+L_g)} & \frac{1}{2(L_2+L_g)} & \omega & \frac{-(3(R_2+R_g)+R_f)}{3(L_2+L_g)} \end{bmatrix}}^{A_{small\ signal}} \begin{bmatrix} \delta v^{cap} \\ \delta i_q^i \\ \delta i_d^i \\ \delta v_q^c \\ \delta v_d^c \\ \delta i_q^o \\ \underbrace{\delta i_d^o}_{\delta x} \end{bmatrix}
$$

$$
+ \underbrace{\begin{bmatrix} \frac{1}{C_{dc}R_s} & 0 & 0 & \frac{-\sqrt{3}}{2C_{dc}}\left[\cos(\Phi)I_q^i+\sin(\Phi)I_d^i\right] & \frac{-\sqrt{3}M}{2C_{dc}}\left[-\sin(\Phi)I_q^i+\cos(\Phi)I_d^i\right] \\ 0 & 0 & 0 & \frac{\sqrt{3}}{3L_1}\left[\cos(\Phi)V^{cap}\right] & \frac{-\sqrt{3}M}{3L_1}\left[\sin(\Phi)V^{cap}\right] \\ 0 & 0 & 0 & \frac{\sqrt{3}}{3L_1}\left[sin(\Phi)V^{cap}\right] & \frac{\sqrt{3}M}{3L_1}\left[cos(\Phi)V^{cap}\right] \\ 0 & 0 & 0 & 0 & 0 \\ 0 & 0 & 0 & 0 & 0 \\ 0 & \frac{-1}{2(L_2+L_g)} & \frac{\sqrt{3}}{6(L_2+L_g)} & 0 & 0 \\ 0 & \frac{-\sqrt{3}}{6(L_2+L_g)} & \frac{-1}{2(L_2+L_g)} & 0 & 0 \end{bmatrix}}_{B_{small\ signal}} \begin{bmatrix} \overbrace{\delta v_{dc} & 0}^{\delta u} \\ 0 & \delta v_q^g \\ 0 & +\delta v_d^g \\ \delta m & 0 \\ \underbrace{\delta\varphi}_{\delta u_c} & \underbrace{0}_{\delta D} \end{bmatrix} \tag{13}
$$

voltage tracking loop can be used for regulating the voltage across the DC-link capacitor or deducing the angle for the converter voltage as in matching control technique and (4). These two functions can be addressed simultaneously and optimally by the MM block. It is worth mentioning that the implementation of two voltage control loops instead of Q-V loop adds more controlled weighting factors in the MM, which enhances the controller degrees of freedom. To sum up, the MM block adds optimum coupling terms between the control loops and maps the effect of each PI output not only to its primary control signal objective but also to other control signals (δv^{dc}, δm, $\delta\varphi$).

In conjunction with this, a full state-feedback controller (gain matrix) will also be designed based on linear quadratic regulator (LQR). This technique helps to optimize the response of the system states, namely, the converter output voltage, converter output power, and DC-link voltage. The design process will be discussed in the following section.

V. MAPPING AND GAIN MATRICES DESIGN

This section explains how the mapping and state-feedback gain matrices are optimally designed to enhance the system performance. Moreover, it discusses the robustness of the proposed controller.

A. FULL STATE-FEEDBACK GAIN MATRIX

The basic idea behind the state-feedback gain controller is to shift all the closed-loop poles (eigenvalues) to certain desired locations. The design of the gain matrix (GM) is based on LQR, which defines the optimal poles location based on an optimized cost function and rather than a certain user-defined location. The LQR technique searches for the state feedback law ($u_c = -kx$) that minimizes the quadratic cost function in (14).

$$J(u_c) = \int_0^\infty \left(x^T Q x + u_c^T Z u_c\right) dt \tag{14}$$

where, Q and Z are the diagonal matrices representing the states deviation and inputs utilization [31] matrices, respectively, and are given in (15).

$$Q = \begin{bmatrix} w_{v_{cap}} & 0 & 0 & 0 & 0 & 0 & 0 \\ 0 & w_{i_q^i} & 0 & 0 & 0 & 0 & 0 \\ 0 & 0 & w_{i_d^i} & 0 & 0 & 0 & 0 \\ 0 & 0 & 0 & w_{v_q^f} & 0 & 0 & 0 \\ 0 & 0 & 0 & 0 & w_{v_d^f} & 0 & 0 \\ 0 & 0 & 0 & 0 & 0 & w_{i_q^o} & 0 \\ 0 & 0 & 0 & 0 & 0 & 0 & w_{i_d^o} \end{bmatrix}$$

$$Z = \begin{bmatrix} w_{\delta v_{dc}} & 0 & 0 & 0 & 0 \\ 0 & 0 & 0 & 0 & 0 \\ 0 & 0 & 0 & 0 & 0 \\ 0 & 0 & 0 & w_{\delta m} & 0 \\ 0 & 0 & 0 & 0 & w_{\delta\varphi} \end{bmatrix} \tag{15}$$

As previously mentioned, GFC operates as a controlled voltage source. So, the concerned states for these converters, which largely affect the system response, such as v^{cap}, v_q^c and v_d^c, will be penalized by increasing the corresponding weighting factors in the Q matrix. Therefore, $w_{v_{cap}}$, $w_{v_q^f}$ and $w_{v_d^f}$ assumed to be 1 and the weighting factors related to the current states such as $w_{i_q^i}$, $w_{i_d^i}$, $w_{i_q^o}$ and $w_{i_d^o}$ assumed to have values less than 1 (the weighting factors related to the current states are assumed to be 0.5 in the proposed method). Similarly, the controllable inputs (actuators) effort can also be penalized by increasing the corresponding weighting factors in the R matrix such as $w_{\delta v_{dc}}$, δm and $\delta\varphi$, which are assumed to be 1. However, the weighting factors corresponding to the uncontrollable inputs (disturbances) will be set to zero. Therefore, the outer control loops with an integral action are designed using PI controllers to counter the grid disturbance effect. Finally, the state feedback gains (K) are obtained by address the objective function in (14), that can be solved using the associated Riccati equation, which discussed in detail in [32], or using MATLAB's function (LQR design). This process is summarized in the following flowchart given in Fig. 8.

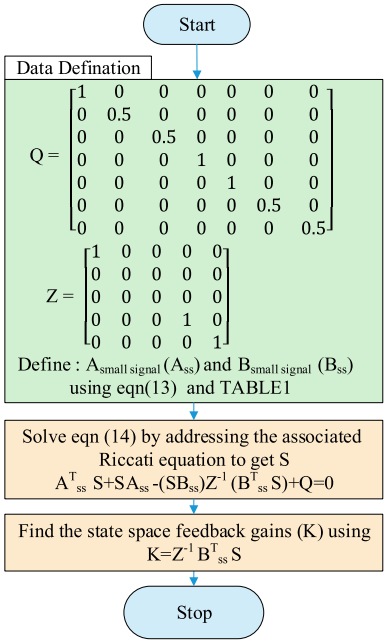

FIGURE 8. LQR design flowchart.

As previously mentioned, the LQR is used for optimally moving the system poles to improve its performance, as shown in Fig. 9, which represents the open loop poles and the closed loop poles/zeros based on the proposed LQR technique for the GFC averaged model. The open loop poles are located near the imaginary axis which yields to a poor damping to the oscillatory components. Table 2 shows that there are three dominant natural frequencies at 589 rad/s, 1033 rad/s and 1781 rad/s with insufficient damping ratios of 76%, 17% and 10%, respectively. By employing the proposed LQR technique, the open loop poles have been moved away from the imaginary axis, as shown in Fig. 9.

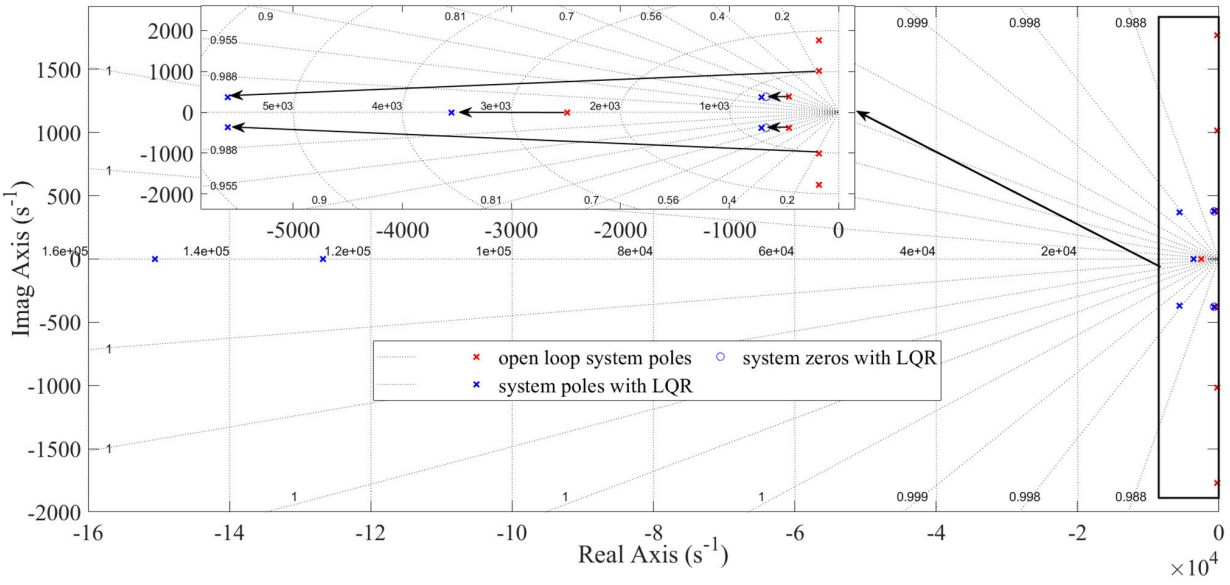

FIGURE 9. Pole-zero map for the open loop and closed loop GFC system based on the proposed controller.

TABLE 2. System open loop characteristics.

poles	Damping ratio %	ω_n (rad/s)	Time constant (ms)
-452+ 377i	76.8	589	2.21
-452- 377i	76.8	589	2.21
-182+ 1017i	17.7	1033	5.47
-182- 1017i	17.7	1033	5.47
-182 + 1771i	10.2	1781	5.49
-182- 1771i	10.2	1781	5.49
-2487	100.0	2487	0.40

TABLE 3. System closed loop characteristics with LQR.

poles	Damping ratio %	ω_n (rad/s)	Time constant (ms)
-706+ 376i	88.2	800	1.42
-706- 376i	88.2	800	1.42
-3551	100	3551	0.28
-5603+ 367i	99.8	5615	0.18
-5603- 367i	99.8	5615	0.18
-126770	100	126770	0.01
-150581	100	150581	0.01

Table 3 shows the better characteristics achieved by LQR. There are three dominant natural frequencies with 800 rad/s, 3551 rad/s and 5615 rad/s with sufficient damping ratios of 88%, 100% and 99%, respectively. Moreover, the nearest poles to the imaginary are cancelled with the proper selection of system zeros, as shown in Fig. 9.

B. MAPPING MATRIX AND PI CONTROLLER DESIGN

PI is a closed loop system and one of the most common controllers that are used to control different plants [33], the mapping matrix given in (16) includes 12 weighting factors, which emulate the required cross-coupling between the control loops and identify the optimum contribution from each PI output control loop.

$$\underbrace{\begin{bmatrix} r_{dc} \\ r_{v_q^g} \\ r_{v_d^g} \\ r_{\mathrm{m}} \\ r_{\phi} \end{bmatrix}}_{r} \underbrace{\begin{bmatrix} -W_{v^{cap}\to v_{dc}} & w_{v_q^f\to v_{dc}} & w_{v_d^f\to v_{dc}} & w_{p_o\to v_{dc}} \\ 0 & 0 & 0 & 0 \\ 0 & 0 & 0 & 0 \\ w_{v^{cap}\to m} & w_{v_q^f\to m} & w_{v_d^f\to m} & w_{p_o\to m} \\ w_{v^{cap}\to \phi} & w_{v_q^f\to \phi} & w_{v_d^f\to \phi} & w_{p_o\to \phi} \end{bmatrix}}_{\text{weighting factors } (5\times4)} \underbrace{\begin{bmatrix} u_{c(dc)} \\ u_{c(vq)} \\ u_{c(vd)} \\ u_{c(p)} \end{bmatrix}}_{u_c 4\times1} \tag{16}$$

where, r is the reference input vector and u_c is the PI output vector.

In conventional damping techniques, the synchronization angle (power angle), ϕ, is estimated using one signal, namely, the control of active power as in VSC or the control of DC-link voltage as in matching control. However, in the proposed damping method, the synchronization angle is calculated using a linear combination between 4 signals, namely, $u_{c(dc)}$ that depends on the DC-link voltage regulation (as in matching control), $u_{c(p)}$ that depends on the regulation of the active power (as in a special type of VSM swing equation) and $u_{c(vd)}/u_{c(vq)}$, that depends on the vd/vq regulation (as in PLL synchronization techniques) as shown in (16). This combined method is more accurate and rapid in estimating the synchronization angle since it depends on the contribution of 4 signals instead of a single signal as in conventional techniques. It is worth mentioning that the inaccurate synchronization will lead to oscillating power flow between the GFC and grid. Therefore, fast and accurate angle estimation will rapidly damp this oscillating power component during transient periods. On the other hand, in conventional damping methods, the change in the GFC output power causes fluctuations in the DC-link voltage, then the DC-DC converter controller

responds and regulates the DC-link voltage according to a feedback from the DC-link voltage. This process remains until the output power from the DC-DC converter matches the power converter output power. However, the proposed damping method uses a feedback signal, which depends on a linear combination between the DC-link voltage, the output converter power, and output converter voltage. This combination ensures that any power mismatch between the DC-DC converter and GFC will be immediately and rapidly balanced with minimum time. Furthermore, in conventional damping methods, the output voltage control through the modulation index of SVPWM assumes that the DC-link voltage is constant without any fluctuations. However, in the proposed damping technique, the modulation index has weighted factors from the DC-link and output power deviations, therefore, it accurately determines the modulation index required for voltage regulation.

PI parameters and mapping matrix are designed in the integrative environment considering the feedback state gains that previously designed using LQR technique [31]. The basic design criterion for tuning the PI controllers and identifying the Mapping matrix is based on addressing the optimization problem given in (17) using pattern search algorithm.

$$\underbrace{min}_{h} f_1(h) = w_1 \left|\Delta v^{cap}\right| + w_2 \left|\Delta v_q^f\right| + w_3 \left|\Delta v_d^f\right| + w_4 \left|\Delta p_o\right| \tag{17}$$

where, h are the decision variables (PI controller constants and MM weighting factors), $w_1 - w_4$ are the weighting factors for the multi-objective function, and $|\Delta v^{cap}|$, $\left|\Delta v_q^c\right|$, $\left|\Delta v_d^c\right|$, $|\Delta p_o|$ represent the absolute error of the concerning responses.

As shown in (17), the objective function includes the deviation of the concerning states for GFC around the reference's values. Pattern search seeks to minimize these deviations, while the system is subjected to wide range of grid disturbances such as: (1) step up/down and swing changes in the grid frequency or voltage, and (2) changes in the active power reference. It is worth mentioning that the minimization of these deviation will improve the damping characteristics of these states. Pattern search strategy can be summed as follows:

Step 1: Setting up an initial condition for the PI parameters and MM.

Step2: The System is simulated using MATLAB/SIMULINK while it subjected to wide range of the grid disturbances.

Step3: The deviations of the concerning states are measured and (17) is calculated.

Step 4: If the value of (17) is fitter than the previously stored value, then this value is stored as a local minimum value.

Step 5: The algorithm seeks to find a better minimum value; therefore, it modifies the PI parameters and MM then go to step (2).

Step 6: The algorithm will repeat step (5) until it achieves the stopping criterion which is considered as maximum number of iterations in which objective function does not minimize anymore, then the recently stored local minimum value is considered as a global minimum. Moreover, the optimization process is described in the flowchart given in Fig. 10. The optimal GM, MM and the optimal PI gains are given in the appendix.

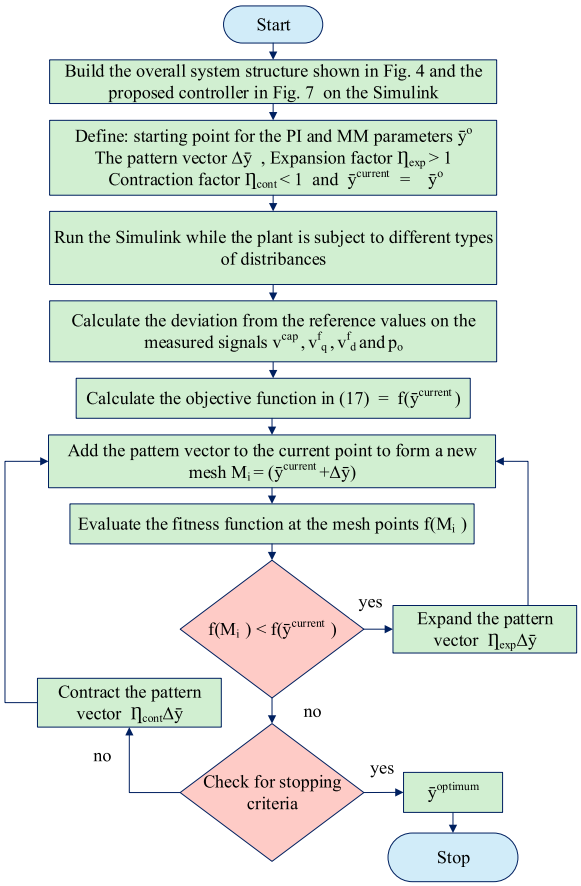

FIGURE 10. PI and MM parameters design flowchart.

C. ROBUSTNESS ANALYSIS OF THE PROPOSED CONTROLLER AGAINST UNCERTAIN SYSTEM PARAMETERS

This subsection discusses the robustness of the proposed controller. There are two common approaches to measure the robustness for the system. (1) Monte-Carlo approach which selects different combinations from the uncertainty ranges of the uncertain parameters then test the system over these combinations. The μ-analysis is implemented using MATLAB software to assess the system robustness. Fig. 11 shows the voltage response of the DC-link capacitor at nominal values set and other 25 random combination sets. Each random set consists of the predetermined uncertain parameters whose values are selected form the uncertainty ranges. It confirms that the voltage response is stable and well-regulated while changing the parameters in the uncertainty ranges, which

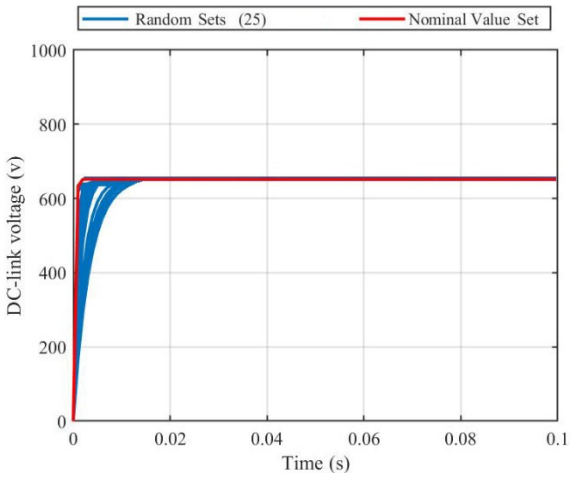

FIGURE 11. The DC-link voltage with parameters uncertainty.

proves that the controller is robustly stable against parameters uncertainty.

This approach can yield a general idea of the system performance over the uncertainty ranges; however, it cannot guarantee the analysis for the worst-case parameter combination. (2) Structured singular value (SSV) approach based on μ-analysis [34]. This analysis guarantees including of the worst-case parameter uncertainty combination. The proposed controller is tested for different possible values of uncertain parameters as listed in Table 4.

TABLE 4. Uncertainty percentage in the system parameters.

Parameters	Nominal value	Uncertainty Range %
C_{dc}	4 mF	25 %
C_f	10 µF	25 %
L_g	2 mH	25 %
L_1, L_2	2.5 mH, 2.5 mH	25 %
R_1, R_2	1 mΩ, 1 mΩ,	25 %
R_f	0.7 Ω	25 %
R_g	3 Ω	25 %
R_s	0.1 Ω	25 %

Moreover, the μ-analysis can search for the instability scenarios outside the uncertainty used ranges ($> 25\%$) if the system is confirmed to be stable inside the uncertainty ranges ($<= 25\%$). There are many parameters' combinations outside the uncertainty ranges that cause instability, therefore, the analysis selects the nearest unstable combination to the nominal values. This combination is listed in Table 5.

Therefore, it is confirmed that the system parameters can be changed up to 56.6% instead of 25% before the instability occurs.

VI. SIMULATION AND CONTROL HARDWARE IN THE LOOP VALIDATION

To validate the proposed controller, a detailed time-domain model of the two-stage grid-connected system given in Fig. 4 is tested for two case studies:

TABLE 5. Small perturbations that cause instability.

Parameters	Value
C_{dc}	6.4 mF
C_f	55.9 µF
L_g	0.568 mH
L_1, L_2	0.96 mH, 4.09 mH
R_1, R_2	0.62 Ω, 0.55 Ω,
R_f	0.215 Ω
R_g	1.301 Ω
R_s	24.7 Ω

The system parameters are shown in Table 1. The first case study is simulated using MATLAB/Simulink software to validate the proposed method against various scenarios of disturbances. In the second case study, the controller is practically validated based on Control Hardware in the loop (CHiL) using OPAL-RT, as shown in Fig. 12. The OPAL-RT platform is operating on 4 cores based on Intel Core Xeon processor at 3 GHz and RAM 2 × 8 GB. The system controller is uploaded on a 150 MHz DSP (Digital Signal Processor) labeled as (TMS320F28335ZJZA). The DSP is responsible for handling the control and feedback signals of GFC setup on OPAL-RT platform. The DSP receives the system states and based on these values it generates the required signals to operate the GFC on OPAL-RT platform. The second study includes a comparison between the conventional PI based control in [11] without (MM and GM), and the proposed damping method. This comparative study clarifies the significance of pre-defined matrices (MM and GM).

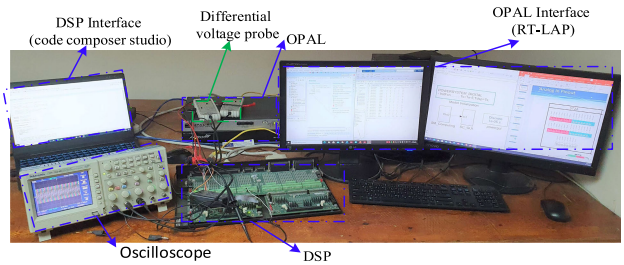

FIGURE 12. Control Hardware in the Loop system.

A. CASE STUDY 1

In this case study, the proposed control method is tested against different disturbances in the grid frequency, grid voltage and converter output power. Fig. 13(a) elucidates the nominal grid frequency with step and swing disturbances at different time instances. Fig. 13(b) illustrates the nominal grid RMS voltage with step disturbances at different time instances. The change in the converter power reference is illustrated in Fig. 13(c). Fig. 14 depicts the responses of the DC-DC converter and grid-connected converter against the different disturbances. The change in the line-line output voltage across the LCL filter capacitor against the disturbances is shown in Fig. 14(a). There are small notches appear on the voltage waveform to support the damping

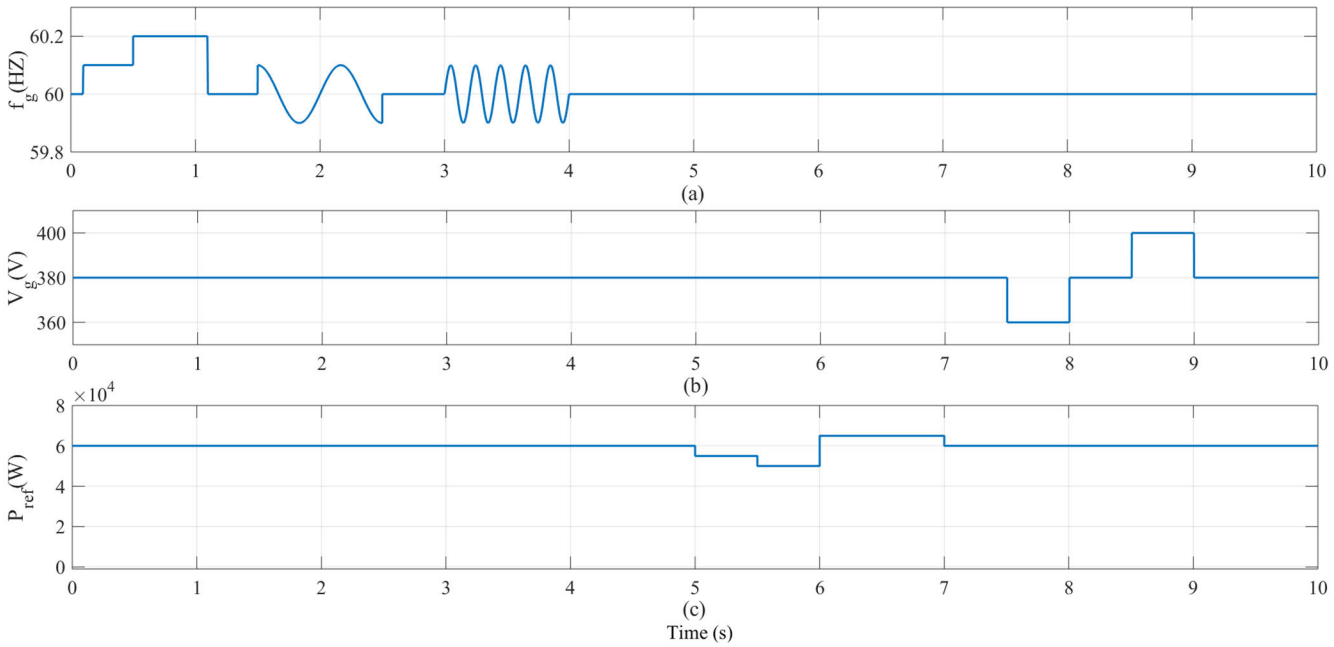

FIGURE 13. Case 1 Grid disturbances: (a) Grid frequency, (b) Grid RMS voltage, and (c) Converter power reference.

process against the disturbances, then remains constant over the whole period. The voltage across the DC-link against the disturbances is shown in Fig. 14(b), which confirms that the DC-link voltage is almost constant even under large voltage and power disturbances. This is simply thanks to using both grid-connected converter and DC-DC converter simultaneously without a communication delay. Therefore, the change in the output converter power causes immediate change in the output DC-DC converter power by the controller. The output converter power response is shown in Fig. 14(c), which exhibits the same inertia response of a conventional SM but with a sufficient damping effect with a maximum power oscillation of 0.1 pu around the nominal power against wide scenarios of disturbances. Also, the converter is smoothly followed the changes in the power reference with a small overshoot/undershoot.

B. CASE STUDY 2

In this study, the proposed damping control method is compared with conventional PI-based damping controller and the results are presented in a per unit basis with respect to the desired values (380 V and 60 kW).

The hardware implementation of the GFC controller is applied using DSP and the OPAL-RT is emulated the grid conditions.

Fig. 15 presents the results against frequency step disturbances, which could be described as follows:

- At t = 0.6 s: a step change occurs from 60 to 60.1Hz;
- At t = 1.1 s: a step change occurs from 60.1 to 60.2 Hz;
- At t = 1.6 s: a sudden drop occurs from 60.2 to 60 Hz;

For a fair comparison, the PI controller gains of the conventional controller are also optimally tuned based on the same pattern search algorithm. As shown in Fig 15(a), a significant improvement in the damping conditions is obtained with the proposed control method over the conventional one. For instance, the worst condition is obtained when the frequency suddenly drops from 60.2 to 60 Hz, where the output power experiences significant oscillations with a maximum amplitude of 3 pu within 0.2 s under conventional PI-based control scheme. With the proposed controller, the output power is quickly damped within 0.05 s with a maximum amplitude of 1.2 pu. This is simply thanks to the MM block, so the damping effect and synchronizing angle are generated based on information from the three possible control loops (active loop, reactive loop, and DC-link loop), while it is usually achieved by only P-f loop in the conventional PI-based control scheme.

Fig. 15(b) presents the output voltage across the filter capacitor and shows the impact of MM on the voltage profile during the disturbances. This proves the claim of reactive loop contributions in the damping process.

Moreover, the system is verified against changing in the output active power, which is another common type of changes in power systems. Fig. 16 presents the responses against the changing of the output active power, which could be described as follows:

- At t = 0.6 s: a sudden drop in the output active power (P) occurs from 1 to 0.65 p.u.;
- At t = 1.1 s: a step change in P occurs from 0.65 to 0.85 p.u.;
- At t = 1.6 s: another step change in P occurs from 0.85 to 1 p.u.;

As shown in Fig 16(a), the damping of the proposed control method is more efficient than the conventional method. For instance, the maximum overshot during this type of

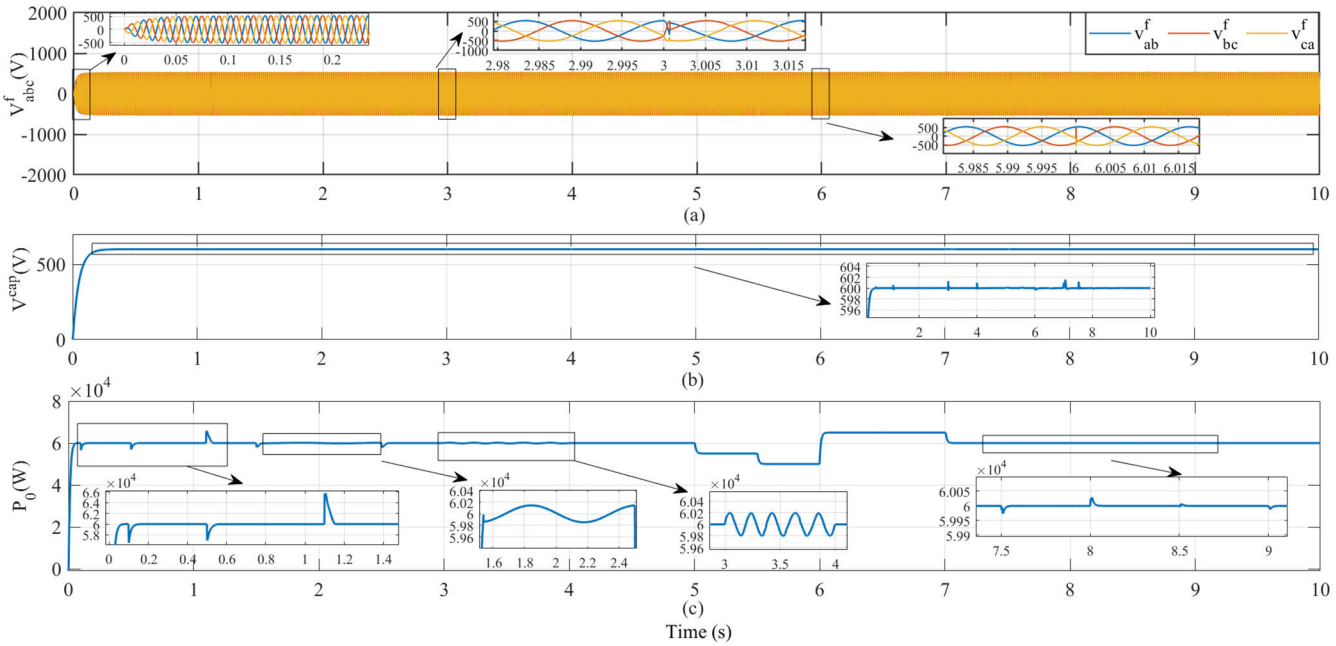

FIGURE 14. Case 1 simulation results under different grid disturbances: (a) Output voltage across the filter capacitor, (b) DC-link voltage, and (c) Converter output power.

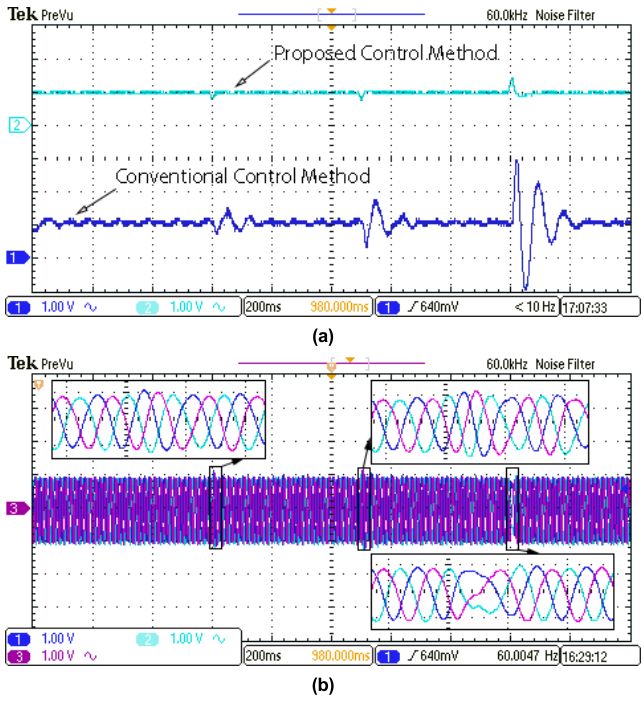

FIGURE 15. Experimental results against frequency disturbances: (a) Top: converter output power for the proposed controller, bottom: converter output power for the conventional controller, and (b) Output voltage across the filter capacitor for the proposed controller.

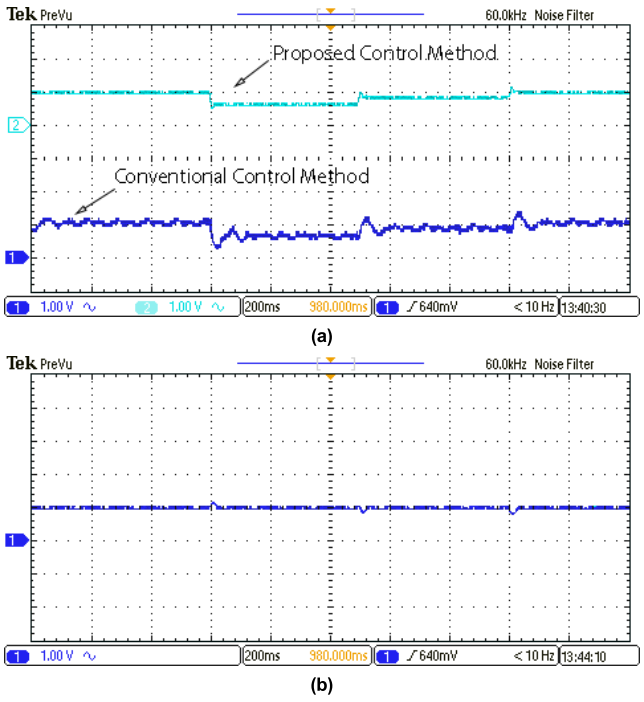

FIGURE 16. Experimental results against active power changes: (a) Top: converter output power for the proposed controller, bottom: converter output power for the conventional controller, and (b) Output voltage across the filter capacitor for the proposed controller.

disturbance is 0.07 p.u. and rapidly damped within 0.02 s, while the overshoot will be worse in the conventional method with 0.2 p.u. and damped within 0.08 s. Fig. 16(b) presents the output voltage across the input DC capacitor and describes the impact of MM on its voltage profile during the changing in the output active power disturbance. It is worth mentioning that the over/under voltage of the DC-link voltage occurs when the inverter output active power does not match the

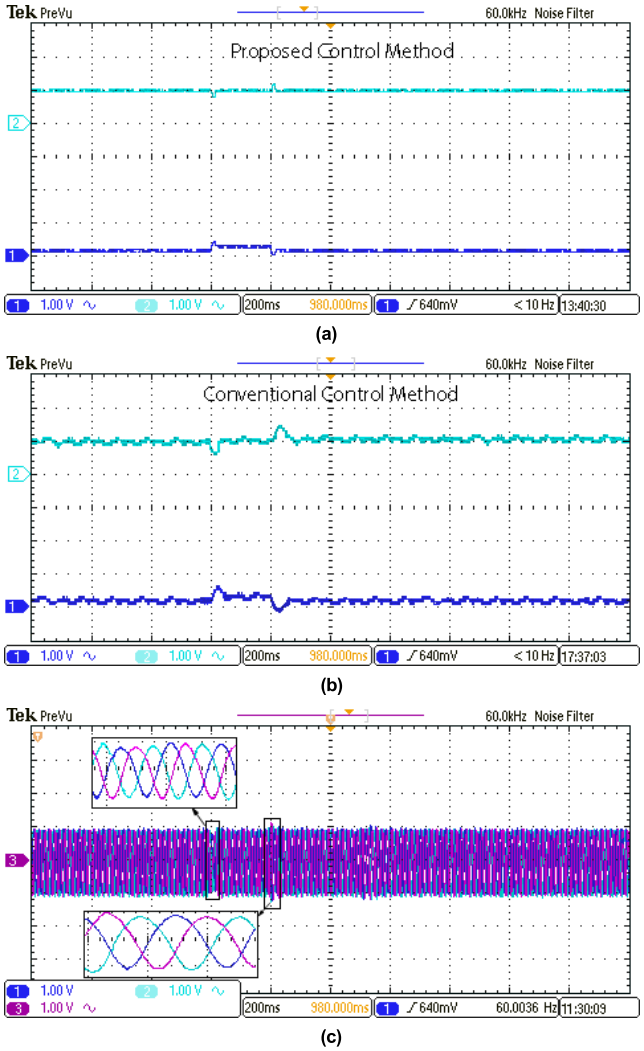

FIGURE 17. Experimental results against disturbances in grid voltage: (a) Top: converter output active power for the proposed controller, bottom: converter output reactive power for the proposed controller, (b) Top: converter output active power for the conventional controller, bottom: converter output reactive power for the conventional controller, and (c) Output voltage across the filter capacitor for the proposed controller.

power from the DC-DC converter. This voltage needs to be rapidly regulated to balance between the inverter and DC-DC converter active powers. Fig. 16(b) shows that the DC-link voltage is rapidly regulated during the power mismatch due to the coupling between the active power and DC regulation loop through MM.

The system is verified as well against disturbances in the grid voltage. Fig. 17 presents the responses of the active and reactive powers against the changing in the grid voltage, which could be described as follows:

- At t = 0.6 s: a sudden drop occurs in the grid voltage (V) from 1 to 0.8 p.u.;
- At t = 0.8 s: a step change in V occurs from 0.8 to 1 p.u.;

As shown in Fig 17(a), the damping of the proposed control method is also more efficient than the conventional method for this type of disturbance. For instance, the maximum overshot during this disturbance is 0.1 p.u. in the active and reactive powers and rapidly damped within 0.01 s. Moreover, the reactive power smoothly increases to support the grid voltage during this drop to preserve the nominal voltage (380V) across the filter capacitor.

In contrast, the overshoot in the conventional method is approximately 0.25 p.u. in the active and reactive powers, and these oscillations are damped within 0.1 s as shown in Fig. 17(b).

Fig. 17(c) presents the output voltage across the filter capacitor and shows that there are some notches during disturbances in the grid voltage however it rapidly returns to its nominal value (380 V) within one cycle 0.0167 s.

As shown in TABLE 6, which summarizes the key findings of this section, the maximum overshoot is significantly curtailed using the proposed damping method compared to the conventional one. The maximum overshoot is reduced by approximately 60% compared to the conventional method against the most common disturbances in the power system, namely, grid frequency, grid voltage and change in the active power demand. Moreover, the oscillations are damped by 10 times faster than the conventional method. Therefore, the proposed damping method introduces more damped responses, which increases the power system stability.

TABLE 6. Comparison between the proposed and conventional damping methods in terms of maximum overshoot and settling time.

Disturbances	Maximum overshoot (pu)		Settling time (s)	
	Proposed Control	Conventional Control	Proposed Control	Conventional Control
Grid Frequency	1.2	3	0.02	0.2
Active Power	0.1	0.25	0.01	0.1
Grid Voltage	0.07	0.2	0.05	0.08

VII. CONCLUSION

An improved damping control method for grid forming converters has been proposed that can be used in low-inertia power systems or inverter dominated microgrid to increase the system stability. The main advantage of the proposed method is that the damping effect and synchronization angle deduction have been contributed by three different terms, namely the converter output voltage, speed (angle), and variation in the DC-link voltage. The proposed damping method has been validated using simulation and Control Hardware in the Loop against different and common types of grid disturbances. The results reflect better and faster damping for the proposed control method against the conventional method. The controller has been optimally designed for a two-stage grid-connected converter coupled by an LCL filter, and it was shown that the damping response can significantly be improved by optimally weighting the three feedback signals using a pattern search algorithm. Moreover, the controller has been tested against parameters uncertainty using μ-analysis, and it was confirmed that the system is robustly stable against variation in the system parameters that

$$A_{0(000)} = \overbrace{\begin{bmatrix} \frac{-1}{C_{dc}R_s} & 0 & 0 & 0 & 0 & 0 & 0 \\ 0 & \frac{-(3R_1+R_f)}{3L_1} & 0 & \frac{-2}{3L_1} & \frac{-1}{3L_1} & \frac{R_f}{3L_1} & 0 \\ 0 & 0 & \frac{-(3R_1+R_f)}{3L_1} & \frac{1}{3L_1} & \frac{-1}{3L_1} & 0 & \frac{R_f}{3L} \\ 0 & \frac{1}{3C_f} & \frac{-1}{3C_f} & 0 & 0 & \frac{-1}{3C_f} & \frac{1}{3C_f} \\ 0 & \frac{1}{3C_f} & \frac{2}{3C_f} & 0 & 0 & \frac{-1}{3C_f} & \frac{-2}{3C_f} \\ 0 & \frac{R_f}{3(L_2+L_g)} & 0 & \frac{2}{3(L_2+L_g)} & \frac{1}{3(L_2+L_g)} & \frac{-(3(R_{2+}R_g)+R_f)}{3(L_2+L_g)} & 0 \\ 0 & 0 & \frac{R_f}{3(L_2+L_g)} & \frac{-1}{3(L_2+L_g)} & \frac{1}{3(L_2+L_g)} & 0 & \frac{-(3(R_{2+}R_g)+R_f)}{3(L_2+L_g)} \end{bmatrix}}^{A_0}$$

$$A_{1(100)} = \overbrace{\begin{bmatrix} \frac{-1}{C_{dc}R_s} & \frac{-1}{C_{dc}} & 0 & 0 & 0 & 0 & 0 \\ \frac{2}{3L_1} & \frac{-(3R_1+R_f)}{3L_1} & 0 & \frac{-2}{3L_1} & \frac{-1}{3L_1} & \frac{R_f}{3L_1} & 0 \\ \frac{-1}{3L} & 0 & \frac{-(3R_1+R_f)}{3L_1} & \frac{1}{3L_1} & \frac{-1}{3L_1} & 0 & \frac{R_f}{3L_1} \\ 0 & \frac{1}{3C_f} & \frac{-1}{3C_f} & 0 & 0 & \frac{-1}{3C_f} & \frac{1}{3C_f} \\ 0 & \frac{1}{3C_f} & \frac{3}{3C_f} & 0 & 0 & \frac{-1}{3C_f} & \frac{-2}{3C_f} \\ 0 & \frac{R_f}{3(L_2+L_g)} & 0 & \frac{2}{3(L_2+L_g)} & \frac{1}{3(L_2+L_g)} & \frac{-(3(R_2+R_g)+R_f)}{3(L_2+L_g)} & 0 \\ 0 & 0 & \frac{R_f}{3(L_2+L_g)} & \frac{-1}{3(L_2+L_g)} & \frac{1}{3(L_2+L_g)} & 0 & \frac{-(3(R_2+R_g)+R_f)}{3(L_2+L_g)} \end{bmatrix}}^{A_1}$$

$$A_{2(110)} = \overbrace{\begin{bmatrix} \frac{-1}{C_{dc}R_s} & \frac{-1}{C_{dc}} & \frac{-1}{C_{dc}} & 0 & 0 & 0 & 0 \\ \frac{1}{3L_1} & \frac{-(3R_1+R_f)}{3L_1} & 0 & \frac{-2}{3L_1} & \frac{-1}{3L_1} & \frac{R_f}{3L_1} & 0 \\ \frac{1}{3L_1} & 0 & \frac{-(3R_1+R_f)}{3L_1} & \frac{1}{3L_1} & \frac{-1}{3L_1} & 0 & \frac{R_f}{3L_1} \\ 0 & \frac{1}{3C_f} & \frac{-1}{3C_f} & 0 & 0 & \frac{-1}{3C_f} & \frac{1}{3C_f} \\ 0 & \frac{1}{3C_f} & \frac{2}{3C_f} & 0 & 0 & \frac{-1}{3C_f} & \frac{-2}{3C_f} \\ 0 & \frac{R_f}{3(L_2+L_g)} & 0 & \frac{2}{3(L_2+L_g)} & \frac{1}{3(L_2+L_g)} & \frac{-(3(R_2+R_g)+R_f)}{3(L_2+L_g)} & 0 \\ 0 & 0 & \frac{R_f}{3(L_2+L_g)} & \frac{-1}{3(L_2+L_g)} & \frac{1}{3(L_2+L_g)} & 0 & \frac{-(3(R_2+R_g)+R_f)}{3(L_2+L_g)} \end{bmatrix}}^{A_2}$$

can be changed up to 56.6 % before the instability occurs. As a future work, the proposed controller will be tested in an inverter-dominated microgrid and the control structure will be supplemented and improved by auxiliary components such as current limitation for fault ride through purposes and to handle unbalanced grid conditions. Moreover, some challenges related to the transient stability for grid-forming power converters will be addressed besides the small signal stability mentioned in this paper.

APPENDIX

The gain matrix can be described using LQR as follows:

$$GM = \begin{bmatrix} 0.42 & 0.05 & -0.01 & 0.02 & -0.02 & -0.06 & 0.01 \\ 0 & 0 & 0 & 0 & 0 & 0 & 0 \\ 0 & 0 & 0 & 0 & 0 & 0 & 0 \\ -0.05 & 0.435 & -0.002 & 0.86 & -0.49 & -0.4 & 0 \\ 0.003 & -0.003 & 0.44 & 0.49 & 0.86 & 0 & -0.4 \end{bmatrix} \tag{A1}$$

The MM can be described using pattern search algorithm as follows:

$$MM = \begin{bmatrix} 1.4075 & 0.0233 & -0.0291 & 0.48 \\ 0 & 0 & 0 & 0 \\ 0 & 0 & 0 & 0 \\ -0.0290 & 0.6393 & -0.3821 & 0.03 \\ 0.234 & 0.0382 & 0.0639 & 0.6395 \end{bmatrix} \tag{A2}$$

The PI parameters are shown as follows $A_{0(000)}, A_{1(100)}, A_{2(110)}$, as shown at the bottom of the previous page

$k_{p1}, k_{p2}, k_{p3}, k_{p4}$	Proportional Gains	0.1, 0.01, 0.01, 0.001
$K_{i1}, k_{i2}, k_{i3}, k_{i4}$	Integral Gains	20, 10, 10, 0.01

REFERENCES

[1] P. Kundur, N. J. Balu, and M. G. Lauby, *Power System Stability and Control*. New York, NY, USA: McGraw-Hill, 1994.

[2] M. Eremia and M. Shahidehpour, *Handbook of Electrical Power System Dynamics: Modeling, Stability, and Control*. Hoboken, NJ, USA: Wiley, 2013.

[3] J. Quintero, V. Vittal, G. T. Heydt, and H. Zhang, "The impact of increased penetration of converter control-based generators on power system modes of oscillation," *IEEE Trans. Power Syst.*, vol. 29, no. 5, pp. 2248–2256, Sep. 2014.

[4] X. Meng, Z. Liu, H. Zheng, and J. Liu, "A universal controller under different operating states for parallel inverters with seamless transfer capability," *IEEE Trans. Power Electron.*, vol. 35, no. 9, pp. 9796–9814, Sep. 2020.

[5] W. Du, Z. Chen, K. P. Schneider, R. H. Lasseter, S. P. Nandanoori, F. K. Tuffner, and S. Kundu, "A comparative study of two widely used grid-forming droop controls on microgrid small-signal stability," *IEEE J. Emerg. Sel. Topics Power Electron.*, vol. 8, no. 2, pp. 963–975, Jun. 2020.

[6] G. Li, Y. Chen, A. Luo, Z. He, H. Wang, Z. Zhu, W. Wu, and L. Zhou, "Analysis and mitigation of subsynchronous resonance in series-compensated grid-connected system controlled by a virtual synchronous generator," *IEEE Trans. Power Electron.*, vol. 35, no. 10, pp. 11096–11107, Oct. 2020.

[7] D. Carletti, A. E. A. Amorim, T. S. Amorim, D. S. L. Simonetti, J. F. Fardin, and L. F. Encarnacao, "Adaptive armature resistance control of virtual synchronous generators to improve power system transient stability," *Energies*, vol. 13, no. 9, p. 2365, May 2020.

[8] M. Ebrahimi, S. A. Khajehoddin, and M. Karimi-Ghartemani, "An improved damping method for virtual synchronous machines," *IEEE Trans. Sustain. Energy*, vol. 10, no. 3, pp. 1491–1500, Jul. 2019.

[9] S. Dong and C. Chen, "Analysis of feasible synchronverter pole-placement region to facilitate parameter tuning," *IEEE Trans. Energy Convers.*, early access, Mar. 24, 2021, doi: 10.1109/TEC.2021.3068758.

[10] M. Ali, H. I. Nurdin, and J. E. Fletcher, "Dispatchable virtual oscillator control for single-phase islanded inverters: Analysis and experiments," *IEEE Trans. Ind. Electron.*, vol. 68, no. 6, pp. 4812–4826, Jun. 2021.

[11] S. Laudahn, J. Seidel, B. Engel, T. Bulo, and D. Premm, "Substitution of synchronous generator based instantaneous frequency control utilizing inverter-coupled DER," in *Proc. IEEE 7th Int. Symp. Power Electron. Distrib. Gener. Syst. (PEDG)*, Jun. 2016, pp. 1–8.

[12] F. Stallmann and A. Mertens, "Sequence impedance modeling of the matching control and comparison with virtual synchronous generator," in *Proc. IEEE 11th Int. Symp. Power Electron. Distrib. Gener. Syst. (PEDG)*, Sep. 2020, pp. 421–428.

[13] F. Milano, F. Dörfler, G. Hug, D. J. Hill, and G. Verbic, "Foundations and challenges of low-inertia systems," in *Proc. Power Syst. Comput. Conf. (PSCC)*, Jun. 2018, pp. 1–25.

[14] L. Huang, H. Xin, Z. Wang, K. Wu, H. Wang, J. Hu, and C. Lu, "A virtual synchronous control for voltage-source converters utilizing dynamics of DC-link capacitor to realize self-synchronization," *IEEE J. Emerg. Sel. Topics Power Electron.*, vol. 5, no. 4, pp. 1565–1577, Dec. 2017.

[15] T. Jouini, C. Arghir, and F. Dörfler, "Grid-friendly matching of synchronous machines by tapping into the DC storage," *IFAC-PapersOnLine*, vol. 49, no. 22, pp. 192–197, 2016.

[16] X. Xiong, C. Wu, B. Hu, D. Pan, and F. Blaabjerg, "Transient damping method for improving the synchronization stability of virtual synchronous generators," *IEEE Trans. Power Electron.*, vol. 36, no. 7, pp. 7820–7831, Jul. 2021.

[17] M. Ndreko, S. Rüberg, and W. Winter, "Grid forming control for stable power systems with up to 100% inverter based generation," in *Proc. 17th Wind Integr. Workshop*, Stockholm, Sweden, 2018, pp. 17–19.

[18] M. A. Hannan, Z. A. Ghani, A. Mohamed, and M. N. Uddin, "Real-time testing of a fuzzy-logic-controller-based grid-connected photovoltaic inverter system," *IEEE Trans. Ind. Appl.*, vol. 51, no. 6, pp. 4775–4784, Nov. 2015.

[19] Z. Li, C. Zang, P. Zeng, H. Yu, S. Li, and J. Bian, "Control of a grid-forming inverter based on sliding-mode and mixed H_2/H_∞ control," *IEEE Trans. Ind. Electron.*, vol. 64, no. 5, pp. 3862–3872, May 2016.

[20] X. Fu and S. Li, "Control of single-phase grid-connected converters with LCL filters using recurrent neural network and conventional control methods," *IEEE Trans. Power Electron.*, vol. 31, no. 7, pp. 5354–5364, Jul. 2016.

[21] T. Qoria, C. Li, K. Oue, F. Gruson, F. Colas, and X. Guillaud, "Direct AC voltage control for grid-forming inverters," *J. Power Electron.*, vol. 20, no. 1, pp. 198–211, Jan. 2020.

[22] X. Yan and S. Y. A. Mohamed, "Comparison of virtual synchronous generators dynamic responses," in *Proc. IEEE 12th Int. Conf. Compat., Power Electron. Power Eng. (CPE-POWERENG)*, Apr. 2018, pp. 1–6.

[23] L. Yang, Y. Chen, A. Luo, Z. Chen, L. Zhou, X. Zhou, W. Wu, W. Tan, and J. M. Guerrero, "Effect of phase-locked loop on small-signal perturbation modelling and stability analysis for three-phase LCL-type inverter connected to weak grid," *IET Renew. Power Gener.*, vol. 13, no. 1, pp. 86–93, Jan. 2019.

[24] G. Yajuan, W. Weiyang, G. Xiaoqiang, and G. Herong, "An improved droop controller for grid-connected voltage source inverter in microgrid," in *Proc. 2nd Int. Symp. Power Electron. Distrib. Gener. Syst.*, Jun. 2010, pp. 823–828.

[25] J. M. Guerrero, L. GarciadeVicuna, J. Matas, M. Castilla, and J. Miret, "A wireless controller to enhance dynamic performance of parallel inverters in distributed generation systems," *IEEE Trans. Power Electron.*, vol. 19, no. 5, pp. 1205–1213, Sep. 2004.

[26] M. Karimi-Ghartemani, S. A. Khajehoddin, P. Piya, and M. Ebrahimi, "Universal controller for three-phase inverters in a microgrid," *IEEE J. Emerg. Sel. Topics Power Electron.*, vol. 4, no. 4, pp. 1342–1353, Dec. 2016.

[27] L. Zhang, L. Harnefors, and H.-P. Nee, "Power-synchronization control of grid-connected voltage-source converters," *IEEE Trans. Power Syst.*, vol. 25, no. 2, pp. 809–820, May 2010.

[28] S. Dong and Y. C. Chen, "Adjusting synchronverter dynamic response speed via damping correction loop," *IEEE Trans. Energy Convers.*, vol. 32, no. 2, pp. 608–619, Jun. 2017.

[29] D. Chen, Y. Xu, and A. Q. Huang, "Integration of DC microgrids as virtual synchronous machines into the AC grid," *IEEE Trans. Ind. Electron.*, vol. 64, no. 9, pp. 7455–7466, Sep. 2017.

[30] P. Unruh, M. Nuschke, P. Strauß, and F. Welck, "Overview on grid-forming inverter control methods," *Energies*, vol. 13, no. 10, p. 2589, May 2020.
[31] E. V. Kumar, J. Jerome, and K. Srikanth, "Algebraic approach for selecting the weighting matrices of linear quadratic regulator," in *Proc. Int. Conf. Green Comput. Commun. Electr. Eng. (ICGCCEE)*, Mar. 2014, pp. 1–6.
[32] V. Kučera, "Algebraic Riccati equation: Hermitian and definite solutions," in *The Riccati Equation*, S. Bittanti, A. J. Laub, and J. C. Willems, Eds. Berlin, Germany: Springer, 1991, pp. 53–88.
[33] R. C. Panda, *Introduction to PID Controllers: Theory, Tuning and Application to Frontier Areas*. Norderstedt, Germany: BoD-Books on Demand, 2012.
[34] S. Sumsurooah, M. Odavic, and S. Bozhko, "μ approach to robust stability domains in the space of parametric uncertainties for a power system with ideal CPL," *IEEE Trans. Power Electron.*, vol. 33, no. 1, pp. 833–844, Feb. 2017.

MOHAMED AHMED received the B.Sc. degree in electrical engineering from Alexandria University, Alexandria, Egypt, in 2016. He is currently a Teaching Assistant with the Mathematics and Applied Physics Department, Faculty of Engineering, Alexandria University. His current research interests include renewable energy, power system control, and power electronics.

FAHAD ALSOKHIRY (Member, IEEE) received the B.Sc. degree (Hons.) in power engineering and electrical machines from King Abdulaziz University, Jeddah, Saudi Arabia, in 2007, and the M.Sc. degree in electrical power engineering with business and the Ph.D. degree in electrical engineering from the University of Strathclyde, Glasgow, U.K., in 2010 and 2016, respectively.

He is currently an Associate Professor with the Electrical and Computer Engineering Department, King Abdulaziz University. He has received research funding as the Principal Investigator on several Research Projects through the Ministry of Education, King Abdullah City for Atomic and Renewable Energy (KACARE) and with King Abdulaziz University. His research interests include HVDC systems, multilevel converters, distributed generation, renewable energy generation, grid integration, and smart grids. He is a member of the IEEE Power and Energy and the Power Electronics Societies and a member of IET.

AYMAN S. ABDEL-KHALIK (Senior Member, IEEE) received the B.Sc. and M.Sc. degrees in electrical engineering from Alexandria University, Alexandria, Egypt, in 2001 and 2004, respectively, and the Ph.D. degree in electrical engineering from Alexandria University and Strathclyde University, Glasgow, U.K., in 2009, under a Dual Channel Program. Since March 2021, he has been appointed as an Academic Visitor at the University of Strathclyde. He is currently a Professor with the Electrical Engineering Department, Faculty of Engineering, Alexandria University. His current research interests include electrical machine design and modeling, electric drives, energy conversion, and renewable energy. He serves as an Associate Editor of IEEE TRANSACTIONS ON INDUSTRIAL ELECTRONICS and *IET Electric Power Applications journal*. Also, he serves as an Executive Editor of *Alexandria Engineering Journal*.

KHALED H. AHMED (Senior Member, IEEE) received the B.Sc. (Hons.) and M.Sc. degrees from Alexandria University, Egypt, in 2002 and 2004, respectively, and the Ph.D. degree in power electronics applications from the University of Strathclyde, U.K., in 2008. Since 2019, he has been appointed as a Professor at Alexandria University. He is currently a Reader in power electronics at the University of Strathclyde. He is a Senior Member of the IEEE Power Electronics and Industrial Electronics Societies. He has published more than 125 technical articles in refereed journals and conferences as well as a published textbook entitled High Voltage Direct Current Transmission: Converters, Systems and DC Grids, a book chapter contribution, and a PCT patent PCT/GB2017/051364. His research interests include renewable energy integration, high-power converters, offshore wind energy, dc/dc converters, HVDC, and smart grids. He serves as a Co-Editor-in-Chief of *Alexandria Engineering Journal* (Elsevier), and as an Associate Editor of IEEE OPEN JOURNAL OF THE INDUSTRIAL ELECTRONICS SOCIETY (OJIES), and IEEE ACCESS.

YUSUF AL-TURKI received the Ph.D. degree in power systems from The University of Manchester, Manchester, U.K., in 1985. Since 1999, he has been a Professor with the Department of Electrical and Computer Engineering, King Abdulaziz University, Jeddah, Saudi Arabia, where he is currently the Dean of Research. His current research interests include system modeling, power system dynamics, renewable energy, and microgrids.